

NeRC: Neural Ranging Correction through Differentiable Moving Horizon Location Estimation

Xu Weng*

Nanyang Technological University
Singapore, Singapore
xu009@e.ntu.edu.sg

K.V. Ling

Nanyang Technological University
Singapore, Singapore
ekvlng@ntu.edu.sg

Haochen Liu

Nanyang Technological University
Singapore, Singapore
haochen002@e.ntu.edu.sg

Bingheng Wang*

National University of Singapore
Singapore, Singapore
wangbingheng@u.nus.edu

Kun Cao

Tongji University
Shanghai, China
caokun@tongji.edu.cn

Abstract

GNSS localization using everyday mobile devices is challenging in urban environments, as ranging errors caused by the complex propagation of satellite signals and low-quality onboard GNSS hardware are blamed for undermining positioning accuracy. Researchers have pinned their hopes on data-driven methods to regress such ranging errors from raw measurements. However, the grueling annotation of ranging errors impedes their pace. This paper presents a robust end-to-end Neural Ranging Correction (NeRC) framework, where localization-related metrics serve as the task objective for training the neural modules. Instead of seeking impractical ranging error labels, we train the neural network using ground-truth locations that are relatively easy to obtain. This functionality is supported by differentiable moving horizon location estimation (MHE) that handles a horizon of measurements for positioning and backpropagates the gradients for training. Even better, as a blessing of end-to-end learning, we propose a new training paradigm using Euclidean Distance Field (EDF) cost maps, which alleviates the demands on labeled locations. We evaluate the proposed NeRC on public benchmarks and our collected datasets, demonstrating its distinguished improvement in positioning accuracy. We also deploy NeRC on the edge to verify its real-time performance for mobile devices.

CCS Concepts

- Information systems → Global positioning systems; • Networks → Location based services.

Keywords

Mobile Devices, GNSS, Localization, End-to-end learning

*Co-corresponding authors.

Permission to make digital or hard copies of all or part of this work for personal or classroom use is granted without fee provided that copies are not made or distributed for profit or commercial advantage and that copies bear this notice and the full citation on the first page. Copyrights for components of this work owned by others than the author(s) must be honored. Abstracting with credit is permitted. To copy otherwise, or republish, to post on servers or to redistribute to lists, requires prior specific permission and/or a fee. Request permissions from permissions@acm.org.

Conference acronym 'XX, Woodstock, NY

© 2018 Copyright held by the owner/author(s). Publication rights licensed to ACM.

ACM ISBN 978-1-4503-XXXX-X/2018/06

https://doi.org/XXXXXXX.XXXXXXX

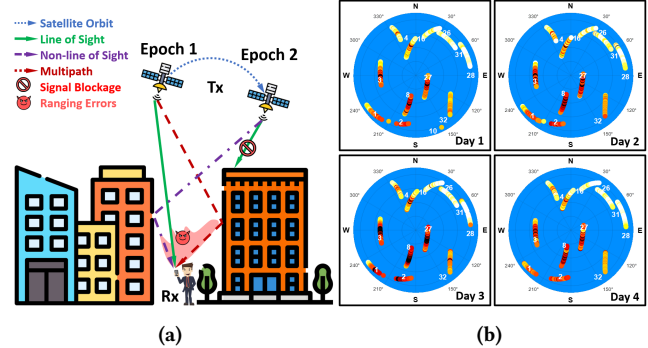


Figure 1: (a) Pervasive multipath/NLOS-induced ranging errors in urban environment. (b) Ranging errors of visible satellites observed at the same site and time across multiple days.

ACM Reference Format:

Xu Weng, K.V. Ling, Haochen Liu, Bingheng Wang, and Kun Cao. 2018. NeRC: Neural Ranging Correction through Differentiable Moving Horizon Location Estimation. In *Proceedings of Make sure to enter the correct conference title from your rights confirmation email (Conference acronym 'XX)*. ACM, New York, NY, USA, 15 pages. <https://doi.org/XXXXXXX.XXXXXXX>

1 Introduction

Global Navigation Satellite Systems (GNSS), a ranging-based wireless positioning system, equips mobile devices with global spatial awareness, serving as a cornerstone for numerous daily applications such as navigation, outdoor augmented reality (AR), city asset management, food delivery, and ride-hailing services. However, particularly for low-cost mobile devices, the complex urban environment poses significant challenges to positioning accuracy [31, 94]. For instance, as shown in Figure 1a, the prevalence of high-rise buildings often reflects or obstructs line-of-sight (LOS) GNSS signals, leading to multipath effects and non-line-of-sight (NLOS) propagation, both of which are longstanding issues that degrade GNSS ranging measurements and compromise positioning accuracy [40, 49, 73, 77]. Additionally, the suboptimal GNSS antennas and chipsets commonly found in commercial mobile devices exacerbate the problem [31, 39, 80, 94].

The ranging errors caused by multipath and NLOS effects are strongly dependent on the complex relationship among satellites

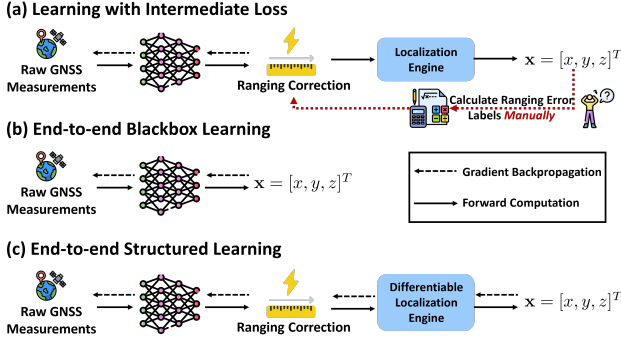


Figure 2: Categories of data-driven ranging error regression

(Tx), receivers (Rx), and the surroundings [62, 64, 81]. Although modeling errors in ranging measurements is challenging, they often exhibit a periodical pattern at a given site because GNSS satellites complete an orbital cycle approximately every 12 hours [1, 51]. Figure 1b shows the periodic ranging errors observed in GNSS data collected with an Android phone at the same site and time across multiple days. The color of each satellite’s trajectory indicates the value of its ranging error, estimated from ground-truth user locations [81] after removing all known error sources, including satellite clock offsets, atmospheric delays, and relativistic effects [29].

The predictability of ranging errors has propelled the community away from traditional model-based approaches [1, 2, 41] toward data-driven methods [62–65, 81, 93]. However, obtaining accurate labels for ranging errors—critical for training neural models—is both difficult and impractical. As illustrated by Figure 2a, previous studies have used various sophisticated algorithms to estimate these errors based on ground truth locations provided by high-performance specialized positioning systems [62, 64, 81, 93]. With the derived ranging errors, an intermediate loss can be computed to train a neural network for ranging correction. Yet, manually calculating ranging errors is inherently imprecise due to the unobservable user clock offsets and stochastic noise [81]. This raises the question: **can we instead utilize these location labels directly, given that our ultimate goal is localization?** If so, we could bypass the need to compute intermediate losses using ranging error labels and instead train neural modules end-to-end with the final positioning task loss.

Motivated by this, researchers have proposed end-to-end neural models to map raw measurements to location corrections directly [28, 46, 95], as illustrated in Figure 2b. Nevertheless, replacing well-established physical or geometric priors with purely neural models turns them into black boxes with limited interpretability. In addition, their positioning accuracy is tightly constrained by the quality of the initial location estimates, to which the corrections are applied, making them susceptible to degraded performance in challenging areas [46, 81], as exemplified by the set transformer in Figure 3.

Can we **integrate** the two learning paradigms (shown in Figure 2a and 2b) to **harness the powerful regression capabilities of neural networks while preserving our interpretable knowledge of GNSS localization?** The key ingredient to enable such

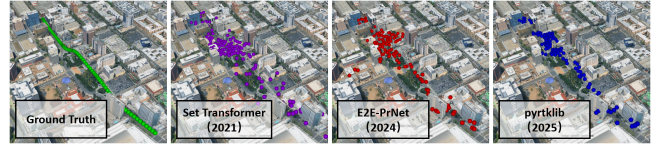


Figure 3: Performance of SOTA end-to-end methods in cities

an end-to-end learning framework should be a differentiable positioning engine, as illustrated in Figure 2c. This engine leverages the outputs from upstream neural models to compute locations while backpropagating gradients from the final positioning task to refine the neural models. This structured learning paradigm, widely adopted in fields such as robotics [70, 72, 89], autonomous driving [25], and 3D vision [5, 44], has recently been extended to GNSS positioning [22, 79, 86, 87]. Among the most relevant studies, E2E-PrNet and pyrtklib train upstream neural network to predict pseudorange errors through a differentiable Weighted Least Squares (WLS) localization engine [22, 79]. While these methods improve positioning in rural [79] or lightly urban areas [22], they struggle in deep urban environments, as shown in Figure 3. The main reason is that the WLS engine lacks robustness to the severe noise present in such settings, where multipath and NLOS propagation typically cause low carrier-to-noise density ratios (C/N_0) [80]. Furthermore, these methods rely solely on fully labeled 3D location data, limiting their practical deployment since obtaining accurate ground-truth locations is both challenging and costly [12].

These challenges raise a key question: **can we build a neural ranging error correction framework trained end-to-end on the final location-related loss, while remaining robust to noise and capable of exploiting unlabeled data?** To address this, we propose a novel Neural Ranging Correction (NeRC) framework. NeRC is trained through differentiable moving horizon location estimation, offering robustness to noise, particularly in urban environments. Moreover, as blessings of end-to-end learning, we further enable training with 2D location data to relax the strict requirement for 3D location labels, and incorporate map-based supervision to unleash the power of unlabeled data. Our main contributions are:

- We design a sequence-to-sequence framework mapping a horizon of raw GNSS measurements to a trajectory of locations. The pipeline comprises an upstream MultiLayer Perceptron (MLP) for ranging error regression and a downstream differentiable localization engine based on Moving Horizon Estimation (MHE).
- We justify the selection of MHE as the downstream location estimator and profile its forward and backward performance.
- We propose training NeRC with only 2D location labels, and further enabling the use of unlabeled data by incorporating supervision from Euclidean Distance Field (EDF) cost maps.
- We comprehensively evaluate NeRC on public smartphone benchmarks and our own collected data, demonstrating that NeRC reaches a new state-of-the-art (SOTA) level in GNSS positioning.
- We deploy NeRC in an edge-based system to enable real-time ranging correction for mobile localization, and extensively profile the system performance, verifying its feasibility in the real world.

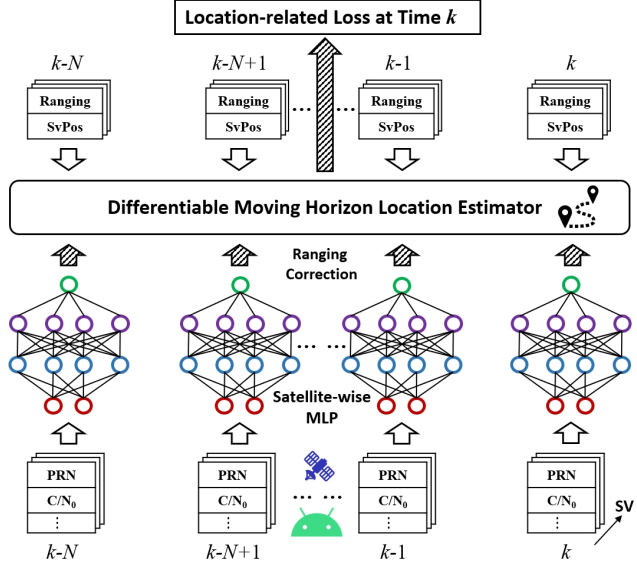


Figure 4: Principle diagram of NeRC.

To the best of our knowledge, this is the first work to learn pseudorange error representations through a differentiable localization engine capable of robust operation in both rural and urban environments. It is also the first to leverage unlabeled GNSS data using publicly available map information. Furthermore, we present a real-world, real-time demonstration of a learning-based mobile system for improving GNSS positioning.

2 NeRC Design

NeRC is a data-driven framework with well-established physical and geometric priors thrown in for ballast. It handles a horizon of raw measurements for neural ranging error regression and robust location estimation. Within it, the neural module is trained with positioning-related metrics. This end-to-end learning pipeline – from raw measurements to locations – comprises two core modules:

- **Upstream Neural Network:** We utilize an MLP to map raw GNSS measurements to pseudorange errors, which serve as one of the inputs to the downstream localization module.
- **Downstream Differentiable Location Estimator:** We design a model-based positioning engine using MHE to handle neural ranging error predictions and track user trajectories robustly, even in noisy urban areas. Its differentiable formulation enables gradients from the location-related loss to propagate backward, allowing end-to-end training of the upstream network.

Figure 4 displays the principal structure of NeRC that processes a horizon of $N + 1$ measurements at time k . N is defined as the horizon size. At each time step, except for the feature dimension, the input data possesses another dimension representing different satellites. For example, as shown by the overlapped data portfolio at time k , the satellite dimension is denoted by SV , which has a size of 32 for the US's GPS constellation. In the following sections, the details of the diagram are explained.

2.1 Upstream Network for Ranging Correction

Considering the SOTA performance of PrNet—an MLP trained with the surrogate intermediate loss—in mobile device GNSS positioning [81], we use a similar MLP backbone as the upstream neural network in NeRC. The MLP is designed to learn the mapping from raw GNSS measurements to pseudorange errors. In addition to the input features mentioned in [81], we include another two features representing the quality of ranging measurements—pseudorange residuals ε_r and their root-sum-squares values E_r [93]. In sum, the input features are denoted by a tensor as follows:

$$\mathbf{I} = \left[C/N_0, \theta_e, PRN, \hat{p}_{LLA}, g_{NED}, \hat{d}_{NED}, \varepsilon_r, E_r \right]^T$$

where C/N_0 is the carrier-to-noise density ratio, and θ_e denotes the elevation angles of visible satellites. PRN refers to the pseudorandom noise codes used as identifiers for GNSS satellites. \hat{p}_{LLA} is the user position estimate from baseline methods like WLS, expressed in the longitude-latitude-altitude (LLA) frame, providing the neural network with awareness of the spatial distribution of ranging errors [62, 64, 81]. g_{NED} denotes the unit vectors from satellites to the user in the north-east-down (NED) frame, capturing the spatial satellite-user geometry. \hat{d}_{NED} is the direction estimation using baseline positioning methods, which to some extent reflects the antenna orientation of mobile devices [81].

Figure 4 illustrates that one input tensor sample has two dimensions corresponding to satellites and features. The MLP operates in a satellite-wise manner—analogous to the position-wise MLPs in the transformer architecture—processing information from all satellites in parallel. A visibility mask handles the time-varying set of visible satellites by zeroing the outputs of invisible ones, analogous to the transformer's masked softmax. For clarity, Figure 4 presents an unfolded view of the input tensors from time $k - N$ to time k . In reality, the NeRC pipeline uses a single MLP that processes the entire time window in parallel. Including the time dimension and the batch dimension for batched training, the resulting four-dimensional input tensor has the shape $B \times (N + 1) \times SV \times I$, where B is the batch size, SV is the total number of satellites, and I is the number of the input features. Thus, the MLP can be represented by

$$\hat{\mathbf{e}}_{k-N:k} = f(\mathbf{I}_{k-N:k}; \Phi) \quad (1)$$

where $\mathbf{I}_{k-N:k}$ denotes the input horizon of size N at time k , $\hat{\mathbf{e}}_{k-N:k}$ is the corresponding pseudorange error predictions, and Φ represents all learnable parameters in the neural network.

2.2 Downstream Location Estimator

2.2.1 Structured Learning Mechanism. Given the ranging correction $\hat{\mathbf{e}}_{k-N:k}$ from the upstream MLP, as shown in Figure 4, combined with other necessary measurements $\Upsilon_{k-N:k}$, including satellite positions, satellite velocities, pseudoranges, and pseudorange rates, the differentiable MHE estimates user trajectories $\hat{\mathbf{x}}_{k-N:k}$ from time $k - N$ to time k , which can be represented by

$$\hat{\mathbf{x}}_{k-N:k} = g(\hat{\mathbf{e}}_{k-N:k}; \Upsilon_{k-N:k}). \quad (2)$$

Let \mathcal{L} denote the location-related loss function. Then, we have the loss value J_k at time k

$$J_k = \mathcal{L}(\hat{\mathbf{x}}_{k-N:k}). \quad (3)$$

Then, composed of (1), (2), and (3), the gradients of the loss with respect to the learnable parameters of the upstream neural network can be expressed using the chain rule:

$$\frac{\partial J_k}{\partial \Phi} = \frac{\partial J_k}{\partial \hat{x}_{k-N:k}} \cdot \frac{\partial \hat{x}_{k-N:k}}{\partial \hat{\epsilon}_{k-N:k}} \cdot \frac{\partial \hat{\epsilon}_{k-N,k}}{\partial \Phi}. \quad (4)$$

On the right side of (4), the first item is normally easy to compute considering the explicit definition of the loss function \mathcal{L} , e.g., the mean squared error loss. The third derivative can be obtained using standard deep learning libraries, such as PyTorch or TensorFlow. The middle one, the derivative of user trajectories with respect to ranging corrections, is derived through differentiable MHE.

2.2.2 Moving Horizon Estimation. We aim to design a robust algorithm to estimate user locations in a GNSS-based system, a NonLinear Time-Variant (NLTV) system, from a bunch of noisy ranging measurements, which can be formulated as

$$\mathbf{x}_{k+1} = f_k(\mathbf{x}_k) + \mathbf{w}_k \quad (5)$$

$$y_k = h_k(\mathbf{x}_k) + \mathbf{v}_k \quad (6)$$

where (5) describes the user dynamics with the process noise term \mathbf{w}_k representing the discrepancy between the modeled dynamics and the actual motion. The measurement equation (6) relates ranging measurements y_k to the user state \mathbf{x}_k , with \mathbf{v}_k representing measurement noise. The initial state of the system is assumed to be a priori, denoted as $\mathbf{x}_0 \sim N(\bar{\mathbf{x}}_0, \mathbf{Q}_{-1})$.

MHE uses a fixed-size window of measurements that slides along the time axis to approximate the full-information state estimation—known as Batched Least Squares (BLS)—which leverages all measurements from the start up to the current time step [48, 56]. MHE is formulated as

$$\begin{aligned} \min_{\{\hat{\mathbf{w}}_{j|k}\}_{k-N-1}^{k-1}} \Phi_k &= \underbrace{\hat{\mathbf{w}}_{k-N-1|k}^T \mathbf{P}_{k-N}^{-1} \hat{\mathbf{w}}_{k-N-1|k}}_{\text{Prior State Cost (Arrival Cost)}} + \\ &\quad \underbrace{\sum_{j=k-N}^{k-1} \hat{\mathbf{w}}_{j|k}^T \mathbf{Q}_j^{-1} \hat{\mathbf{w}}_{j|k}}_{\text{State Transition Cost}} + \underbrace{\sum_{j=k-N}^k \hat{\mathbf{v}}_{j|k}^T \mathbf{R}_j^{-1} \hat{\mathbf{v}}_{j|k}}_{\text{Measurement Cost}} \\ \text{s.t. : } \hat{\mathbf{w}}_{k-N-1|k} &= \hat{\mathbf{x}}_{k-N|k} - \hat{\mathbf{x}}_{k-N|k-N-1} \\ \hat{\mathbf{w}}_{j|k} &= \hat{\mathbf{x}}_{j+1|k} - f_j(\hat{\mathbf{x}}_{j|k}) \\ \hat{\mathbf{v}}_{j|k} &= \hat{\mathbf{y}}_j - h_j(\hat{\mathbf{x}}_{j|k}) \end{aligned} \quad (7)$$

where $[\hat{\cdot}]_{j|k}$ denotes an estimate of an unknown at time j given measurements up to time k . \mathbf{Q}_j and \mathbf{R}_j represent the covariance matrices of process and measurement noise, respectively. The inverse of them is used to weight the state transition and measurement costs. \mathbf{P}_{k-N} is the covariance matrix of the state estimation $\hat{\mathbf{x}}_{k-N|k-N-1}$, representing prior knowledge of our confidence in the initial user state for the current horizon $[k-N, k]$. It also represents the “inertia” of the system—a larger \mathbf{P}_{k-N}^{-1} increases the contribution of the prior state cost in the overall objective, thereby drawing the state estimates in the current horizon more consistent with historical trajectories. Assuming the system statistics in (7) are Gaussian, MHE formulated by (7) is equivalent to the Maximum A Posteriori

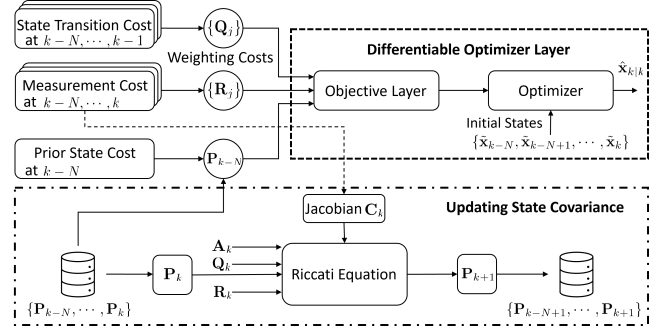


Figure 5: Principle diagram of differentiable MHE. It comprises three layers: the cost computation layer, the differentiable optimizer layer, and the state covariance update layer.

(MAP) estimation [26, 82]:

$$\max_{\{\hat{\mathbf{x}}_{j|k}\}_{k-N}^k} p(\mathbf{x}_{k-N}, \dots, \mathbf{x}_k | \mathbf{y}_{k-N}, \dots, \mathbf{y}_k). \quad (8)$$

2.2.3 Differentiable Formulation of MHE. We estimate the user location $[x_k, y_k, z_k]^T$, velocity $[v_{x_k}, v_{y_k}, v_{z_k}]^T$, receiver clock offset δt_{u_k} , and clock drift δf_{u_k} simultaneously:

$$\mathbf{x}_k = [x_k, v_{x_k}, y_k, v_{y_k}, z_k, v_{z_k}, \delta t_{u_k}, \delta f_{u_k}]^T. \quad (9)$$

Considering the low dynamics of daily mobile devices, the system dynamics between consecutive time samples is typically simplified as uniform rectilinear motion. So, the nonlinear function $f_k(\cdot)$ in (5) becomes a linear coefficient matrix \mathbf{A}_k :

$$f_k(\cdot) = \mathbf{A}_k = \text{diag}\{\mathbf{A}_{0k}, \mathbf{A}_{0k}, \mathbf{A}_{0k}, \mathbf{A}_{0k}\}, \quad \mathbf{A}_{0k} = \begin{bmatrix} 1 & T_k \\ 0 & 1 \end{bmatrix} \quad (10)$$

where T_k is the sampling interval between time k and $k+1$. Two types of ranging measurements are embodied by \mathbf{y}_k , i.e., pseudoranges $\rho_k^{(n)}$ and pseudorange rates $\dot{\rho}_k^{(n)}$, where $[\cdot]_k^{(n)}$ denotes the measurement of the satellite n at time k . Pseudorange rates are normally accurate enough for velocity estimation, so we only regress pseudorange errors $\epsilon_k^{(n)}$ for better location estimation. The satellite clock offsets, relativistic effects, and atmospheric delays were removed from pseudorange measurements during data preprocessing [29]. Therefore, \mathbf{y}_k is written as:

$$\left[\rho_k^{(1)} - \hat{\epsilon}_k^{(1)}, \dot{\rho}_k^{(1)}, \dots, \rho_k^{(M)} - \hat{\epsilon}_k^{(M)}, \dot{\rho}_k^{(M)} \right]^T \quad (11)$$

where M is the total number of visible satellites at time k . The relationship between the user state and ranging measurements, the nonlinear function $h_k(\cdot)$ in (6), can be modeled as [47]:

$$\rho_k^{(n)} = \|\mathbf{p}_k - \mathbf{p}_k^{(n)}\| + \delta t_{u_k} \quad (12)$$

$$\dot{\rho}_k^{(n)} = (\mathbf{v}_k - \mathbf{v}_k^{(n)}) \cdot \mathbf{g}_k^{(n)} + \delta f_{u_k} \quad (13)$$

where $\mathbf{p}_k^{(n)}$ and $\mathbf{v}_k^{(n)}$ represents the location and velocity of satellite n at time k . $\mathbf{g}_k^{(n)}$ is the unit geometry vector from satellite n to the user at time k , which is computed as:

$$\mathbf{g}_k^{(n)} = \left[\tilde{x}_k - x_k^{(n)}, \tilde{y}_k - y_k^{(n)}, \tilde{z}_k - z_k^{(n)} \right]^T / \tilde{r}_k^{(n)}$$

where $\tilde{\mathbf{p}}_k = [\tilde{x}_k, \tilde{y}_k, \tilde{z}_k]^T$ is the approximate user location guess for system initialization. $\tilde{r}_k^{(n)}$ denotes the geometry distance between the satellite n and the location $\tilde{\mathbf{p}}_k$.

We adaptively compute the covariance matrix $\{Q_j\}_{k-N}^{k-1}$ of process noise using a two-state model with two integrals that transfer disturbance (or accelerations) to state displacements [61]. For the measurement noise covariance matrix $\{R_j\}_{k-N}^k$, we construct it as a diagonal matrix by placing the 1-sigma uncertainties of ranging measurements provided by mobile devices on its main diagonal. To approximate the full-information estimator that uses measurements since time zero, the covariance matrix P_{k-N} is computed recursively using the linear discrete filtering Riccati equation [56]:

$$\mathbf{P}_{k+1} = \mathbf{Q}_k + \mathbf{A}_k [\mathbf{P}_k - \mathbf{P}_k \mathbf{C}_k^T (\mathbf{C}_k \mathbf{P}_k \mathbf{C}_k^T + \mathbf{R}_k)^{-1} \mathbf{C}_k \mathbf{P}_k] \mathbf{A}_k^T \quad (14)$$

where \mathbf{P}_0 is considered as prior knowledge and is initiated using a diagonal matrix with all elements on its diagonal equal to 0.05. \mathbf{C}_k is the Jacobian matrix of the nonlinear function $h_k(\mathbf{x}_k)$:

$$\mathbf{C}_k = \begin{bmatrix} \tilde{a}_{x_k}^{(1)} & 0 & \tilde{a}_{y_k}^{(1)} & 0 & \tilde{a}_{z_k}^{(1)} & 0 & 1 & 0 \\ 0 & \tilde{a}_{x_k}^{(1)} & 0 & \tilde{a}_{y_k}^{(1)} & 0 & \tilde{a}_{z_k}^{(1)} & 0 & 1 \\ \vdots & \vdots \\ \tilde{a}_{x_k}^{(M)} & 0 & \tilde{a}_{y_k}^{(M)} & 0 & \tilde{a}_{z_k}^{(M)} & 0 & 1 & 0 \\ 0 & \tilde{a}_{x_k}^{(M)} & 0 & \tilde{a}_{y_k}^{(M)} & 0 & \tilde{a}_{z_k}^{(M)} & 0 & 1 \end{bmatrix} \quad (15)$$

where $\tilde{a}_{x_k}^{(n)}$, $\tilde{a}_{y_k}^{(n)}$, and $\tilde{a}_{z_k}^{(n)}$ are the three elements of $\mathbf{g}_k^{(n)}$ in turn. The prior state $\tilde{\mathbf{x}}_{k-N|k-N-1}$ is considered known for the current horizon at time k and computed using (5) given the previous state estimate $\tilde{\mathbf{x}}_{k-N-1|k-N-1}$. Now, we have all the parts required for the moving horizon location estimation.

Figure 5 illustrates the principle of the differentiable MHE. By substituting (9), (10), (11), (12), and (13) into (7), we obtain the state transition cost, measurement cost, and prior state cost. The objective layer aggregates the three types of costs weighted by their corresponding covariance matrices, which is then solved by a general Differentiable Nonlinear Least Squares (DNLS) solver. In our implementation, we employ the Theseus library built for Pytorch [52]. The optimizer is initialized with an approximate trajectory guess, denoted by $\{\tilde{\mathbf{x}}_{k-N}, \dots, \tilde{\mathbf{x}}_k\}$, for each horizon. We leverage the historical state estimates $\{\tilde{\mathbf{x}}_{k-N|k-N-1}, \dots, \tilde{\mathbf{x}}_{k|k-1}\}$ as the approximate trajectory [82]. The lower half of this diagram depicts the updating process of the prior state covariance matrix using (14), where only the latest covariance matrix \mathbf{P}_k gets updated at time k . The updated horizon of covariance matrices $\{\mathbf{P}_{k-N+1}, \dots, \mathbf{P}_{k+1}\}$ serves the next $N+1$ horizons.

In this section, instead of intuitively using a sliding window mechanism, we design a localization engine based on the state space model and moving horizon estimation. In the following section, we profile its forward and backward performance.

3 Unification and Profiling

3.1 Unification

Why do we choose MHE as the positioning engine rather than the classic Extended Kalman Filter (EKF) or the popular Factor Graph Optimization (FGO)? The underlying reason is

that the MHE framework can unify the other two algorithms. Their equivalence can be established as follows:

- **EKF:** Under certain prerequisites about the initial trajectories and disturbance statistics of an NLTV system, a recursive expression for MHE can be analytically derived, formulating a filtering-based MHE and establishing the equivalence between them, regardless of the horizon size [82].
- **FGO:** If the statistics of an NLTV system are Gaussian, FGO will be equivalent to MHE [26]. However, in GNSS localization, FGO is typically implemented in the absence of the prior state factor [75, 87, 99]. In the following analysis, FGO refers to an MHE without the arrival cost.

Therefore, we provide a comparative study of **the filtering-based MHE (MHE-F)**, **the optimization-based MHE without the arrival cost (MHE-w/o-AC)**, and **the optimization-based MHE with the arrival cost (MHE-w/-AC)** in terms of forward positioning and backward training in the following sections. For a fair comparison, they are implemented with the **same** system model, disturbance statistics, and initial conditions. A public dataset collected by Pixel 4 in deep urban regions is used for evaluation.

3.2 Forward profiling

First, we profile them as standalone positioning engines, without any neural modules involved. The forward testing loss (positioning errors) and computational time are shown in Figure 6a and 6b.

Figure 6a indicates that MHE-w/-AC maintains a lead over other algorithms as the horizon size is small. Unlike the filtering-based MHE-F, which executes a single-pass update at each step, MHE-w/-AC adopts an optimization-based approach that iteratively processes the measurements at every time step. Although MHE-w/o-AC also follows an optimization-based strategy, it only leverages measurements within the current horizon, disregarding prior information. This omission significantly degrades its performance in short horizons. Increasing the horizon size can narrow down the performance gap between MHE-w/-AC and MHE-w/o-AC. Once the horizon extends beyond a certain threshold—approximately 65 in this example—MHE-w/o-AC begins to outperform MHE-w/-AC. At that point, the window is sufficiently long to retain informative measurements for current-state estimation, while older data outside the window degrades performance [33, 34, 82]. Nevertheless, continuously increasing the horizon size does not always lead to improved performance. A typical performance curve of MHE-w/o-AC initially decreases to a minimum, then gradually converges back toward that of MHE-w/-AC [54, 82]. In this dataset, we observe that the turning point occurs at a horizon length of approximately 450. The filtering-based MHE-F exhibits the same performance regardless of the chosen horizon size [48, 82].

Regarding the computation time of each method, Figure 6b shows that the forward time increases as the horizon size enlarges. Among the methods, MHE-F demonstrates the fastest performance, benefiting from its recursive filtering structure. In contrast, the optimization-based approaches are naturally slower, as they solve a nonlinear least squares problem at each time step. Notably, MHE-w/-AC incurs slightly more computation than MHE-w/o-AC for the same horizon size, due to the additional optimization involved in incorporating the arrival cost. However, MHE-w/-AC can achieve

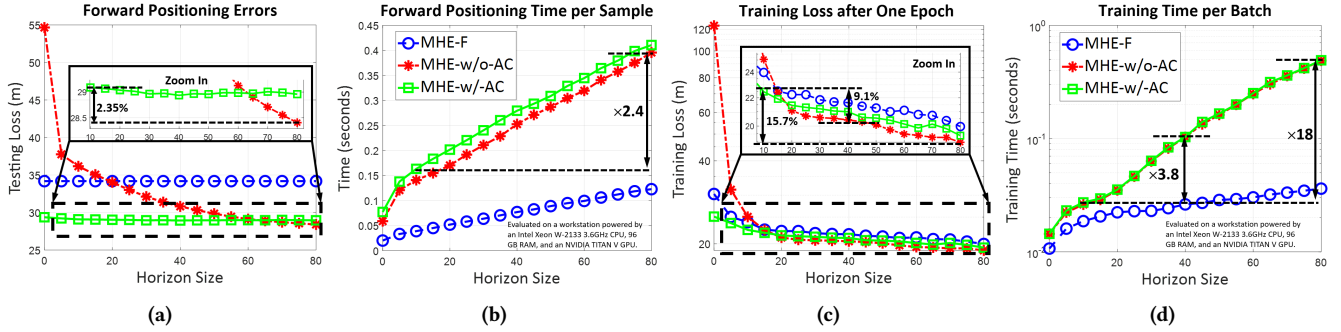


Figure 6: Forward and backward profiling of the filtering-based MHE (MHE-F), the MHE without arrival cost (MHE-w/o-AC), and the MHE with arrival cost (MHE-w/-AC) under various horizon sizes.

superior positioning accuracy with a smaller horizon, thereby taking less computational time to reach similar performance levels.

Summary: MHE offers advanced positioning capabilities at a competitive cost, making it an attractive choice for downstream positioning engines. Although increasing the horizon size can further enhance the accuracy of MHE-w/o-AC, the marginal gains over MHE-w/-AC with a smaller horizon come with a substantial rise in computational time—a 2.35% improvement in accuracy comes at the expense of approximately 2.4 times the computation time, as shown in Figure 6a and Figure 6b. This trade-off is critical to consider when deploying MHE on resource-constrained platforms such as mobile devices. Additional improvement in MHE is outside the scope of this paper, but can be expected by approximating the arrival cost more accurately [11, 53, 56, 67] and incorporating constraints on the system [16, 55, 66, 75, 83].

3.3 Backward profiling

This section investigates the training convergence of the upstream MLP equipped with MHE. Figure 6c gives the training loss (3D location loss) after one training epoch for various horizon sizes.

Increasing the horizon size improves training convergence across all estimators. While MHE-w/o-AC exhibits poor convergence at small horizons, it surpasses the other two methods in convergence speed once the horizon exceeds 20, as illustrated in Figure 6c. It is the arrival cost item in (7)—the system’s ‘inertia’—that decelerates the backward convergence of MHE-F and MHE-w/-AC. Interestingly, it is the same item that enables MHE to achieve satisfactory forward positioning accuracy even with small horizon sizes. Among the two estimators that incorporate the arrival cost, MHE-w/-AC demonstrates better convergence performance than MHE-F, benefiting from its improved positioning accuracy.

Figure 6d shows the backward training time per batch of the three methods. Just aligned with the forward time, MHE-F exhibits the lowest backward computation time due to its filtering structure. In contrast, both MHE-w/-AC and MHE-w/o-AC exhibit increasingly higher computational costs as the horizon size grows.

Summary: The backward training convergence can be improved by expanding the receding horizon, which is equivalent to reducing the contribution of the arrival cost in the overall optimization objective (7). However, increasing the horizon size extends the training

time. For instance, achieving a 9.1% gain in training loss convergence requires approximately 3.8 times more training time, while a 15.7% improvement demands nearly an 18-fold increase in training time. As the horizon grows, the marginal gain in convergence shrinks while the marginal cost in training time grows steeply, which is a trade-off that requires a balance.

4 Training NeRC

We train a separate NeRC for each area or route, just like other data-driven regression paradigms that tightly depend on the specific scenes in which they are applied [44, 97, 98]. Additionally, a separate NeRC model is also trained for each specific time interval of the day, as GNSS satellites (Tx) orbit the Earth periodically. In this section, we discuss how to train the NeRC pipeline. In addition to supervised learning using GNSS data labeled with ground truth locations, we propose an alternative training paradigm to unleash the power of unlabeled data.

4.1 Supervised Learning

It is standard and direct to use ground truth locations to train an end-to-end learning pipeline for localization [28, 79]. The supervised training loss is shown as follows.

$$\mathcal{L}_{3D} = \|\hat{\mathbf{p}}_k - \mathbf{p}_k\|^2 \quad (16)$$

where the location label \mathbf{p}_k can be collected using high-performance geodetic integrated positioning systems like NovAtel’s SPAN system [12, 21]. The traditional data-driven ranging correction methods, which use intermediate training loss, also require labels of user clock offsets [62, 81, 93]. However, tracking user clock offsets is challenging [81, 84]. By contrast, as a benefit of end-to-end learning for localization, NeRC can be trained without them. It is also worth noting that supervising user velocities and clock drifts is unnecessary because the corresponding ranging rate measurements are accurate enough, requiring no further corrections.

Similarly, we can further eliminate the vertical location labels (altitudes) from the training process for two main reasons:

- It is also challenging to label the altitude, even with specialized high-performance positioning systems [29].
- We are more concerned about the horizontal positioning performance of mobile devices.

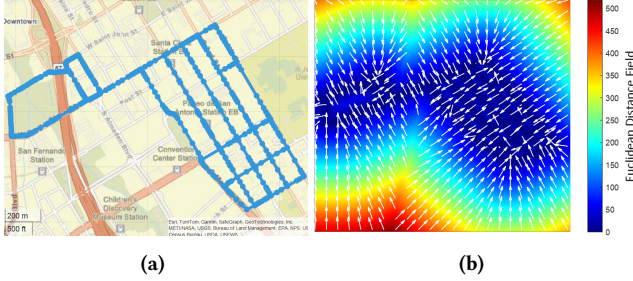


Figure 7: (a) Routes extracted from Google Maps and (b) its Euclidean distance field cost map. The white arrows indicate the gradient descending directions of the cost.

In GSDC 2022, Google removed the vertical labels and pushed researchers to focus on horizontal localization. As a blessing of end-to-end learning, NeRC allows the training with only 2D horizontal labels, thereby avoiding the use of inaccurate labels for altitudes. Let ϕ_k and λ_k respectively denote the ground truth latitude and longitude of a user at time k . Then, we get the 2D training loss:

$$\mathcal{L}_{2D} = \|[\hat{\phi}_k, \hat{\lambda}_k]^T - [\phi_k, \lambda_k]^T\|^2 \quad (17)$$

where

$$[\hat{\phi}_k, \hat{\lambda}_k]^T = f_{ECEF2LLA}(\hat{p}_k)$$

where $f_{ECEF2LLA}$ represents the conversion of user locations from the ECEF coordinate system to the LLA frame, which is differentiable and can be integrated into the learning pipeline [29].

4.2 Unleashing the Power of Unlabeled Data

Innumerable unlabeled GNSS data are generated from mobile devices every day, but have never been fully used. **As the blessings of end-to-end learning**, we propose a brand new learning paradigm using Euclidean Distance Field (EDF) cost maps to unleash the power of unlabeled GNSS data. The core idea behind this innovation is to construct a differentiable map supervision by comparing the predicted trajectories with the passable routes provided by publicly available geodetic maps, like Google Maps or OpenStreetMap. This novel learning paradigm is inspired by robot motion planning [15, 57, 90], robust flight control (actual–reference trajectory comparison) [70], and map matching [42, 50].

We assume that a user travels along the passable routes in an area. As shown in Figure 7a, we can extract passable routes from Google Maps and construct a corresponding spatial cost function. The design principle is to ensure a lower cost value as the user's trajectory becomes more aligned with the reference route. To this end, we propose to employ the Euclidean distance from each predicted location to its nearest reference route as the cost to supervise the learning process. This can be done through the Euclidean distance transform (EDT) of the map as illustrated by Figure 7b, which is referred to as the Euclidean distance field (EDF) cost map [15, 90]. For each spatial point p on the map, EDT produces a potential value $\mathcal{D}(p)$ representing the distance between p and its nearest point on the reference route \mathcal{G} [10]:

$$\mathcal{D}(p) = \min_{q \in \mathcal{G}} (\|p - q\|_2)$$

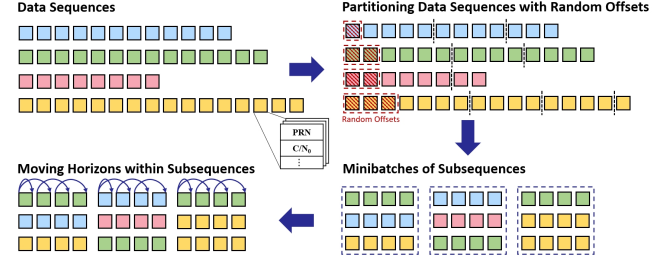


Figure 8: Sequential data loader for training NeRC

where q denotes a point on the reference route \mathcal{G} . For the user trajectory in the horizon at time k , the EDF training loss is:

$$\mathcal{L}_{EDF} = \frac{1}{N+1} \sum_{i=k-N}^k \mathcal{D}(\hat{p}_i). \quad (18)$$

The gradient descending directions of the cost map are illustrated by the white arrows in Figure 7b. The gradient information of the cost always pushes the location prediction toward the reference trajectory, which is a dual analogy for collision avoidance in robot motion planning [15, 57, 90].

5 NeRC Implementations

NeRC is a sequence-to-sequence data-driven framework comprising an upstream MLP and a differentiable downstream MHE. We leverage PyTorch and Theseus to implement them. The specific configurations are listed below.

5.1 Sequential Data Loader

Drawing inspiration from the techniques of random sampling and sequential partitioning used for reading long sequence data in natural language processing [92], we design a sequential data loader tailored for handling raw GNSS measurements, as illustrated in Figure 8. Long sequences from the data files are first truncated using random offsets and subsequently divided into equal-length subsequences. These subsequences serve as the fundamental units, which are then randomly assembled into mini-batches. Finally, a sliding window moves along the batched subsequences to perform moving horizon estimation.

5.2 MLP Configuration

We adopt the parameter settings of the SOTA PrNet [81] to build the upstream neural network—a 40-layer MLP with 20 hidden neurons per layer, using ReLU as the activation function. The MLP is initialized with values drawn from a Kaiming normal distribution [17]. For training the upstream network, we use the Adam optimizer with a learning rate that starts at 0.01 and decays over time. Training NeRC is typically efficient, converging within minutes to a few hours, depending on the scale of the training data.

5.3 MHE Configuration

The differentiable MHE is empowered by Theseus, a DNLs solver built for PyTorch [52]. The Gauss-Newton optimizer is selected as the optimization kernel, with the maximum number of iterations

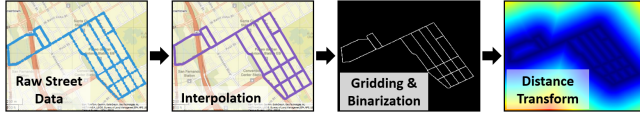


Figure 9: The pipeline of Euclidean distance field cost map computation. Raw street data is from Google My Maps.

and step size empirically tuned for optimal performance. Specifically, we set the step size to 0.5 and limit the number of iterations to 10. To balance the trade-off between training performance and efficiency, as indicated by Figure 6, we eliminate the arrival cost and set the horizon size to 15. During inference, we employ the MHE with the arrival cost and set the horizon size to 5.

5.4 Building Euclidean Distance Cost Maps

The workflow of constructing an EDF cost map is illustrated by Figure 9. We start with collecting raw reference street data using Google My Maps, where walking, biking, and driving routes are freely available. Such data can be exported as a file of waypoints in the Keyhole Markup Language (KML) format. However, the raw street waypoints are too sparse to provide efficient supervision. Thus, we leverage the cubic spline to interpolate these raw route waypoints to obtain a dense and smooth reference route. Then, we grid the interpolated map on the longitude-latitude lattice with a tunable resolution. The grid cells occupied by the passable route are set to 1, while the blocked cells are set to 0. In this way, the gridded map turns into a binary image for efficient Euclidean distance transform (EDT) computation. Many mature solutions to computing the EDT of binary images are available [3, 10, 43, 50]. We use the `bwdist` method provided by MATLAB to compute the Euclidean distance field (EDF) of the gridded map. To make the EDF cost map more differentiable, we apply to the map matrix a Gaussian lowpass filter of size 5 with a standard deviation of 1 [90]. Then, we compute the loss function (18) using PyTorch’s `grid_sample` method.

6 Evaluation

This section presents a comprehensive quantitative evaluation of NeRC’s localization performance using real-world datasets.

6.1 Datasets

The GSDC datasets are publicly available [12, 13] and provide a large volume of data collected **repeatedly along consistent routes and within similar time intervals of days**, making them ideal benchmarks for evaluating NeRC’s performance. Accordingly, we leverage both the GSDC datasets and our own collected data (Figure 10) to construct a range of evaluation scenarios. Unlike previous studies that relied solely on fully labeled datasets [28, 81, 87, 95], **our approach also exploits partially labeled data (with 2D annotations) and even unlabeled data**. A summary of the datasets used in our evaluation is presented in Table 1.

GSDC 2021: The dataset consists of raw GNSS measurements collected across the Mountain View and San Jose cities, covering both open and urban areas. Ground truth positions are fully labeled using the NovAtel SPAN integrated navigation system [12]. We

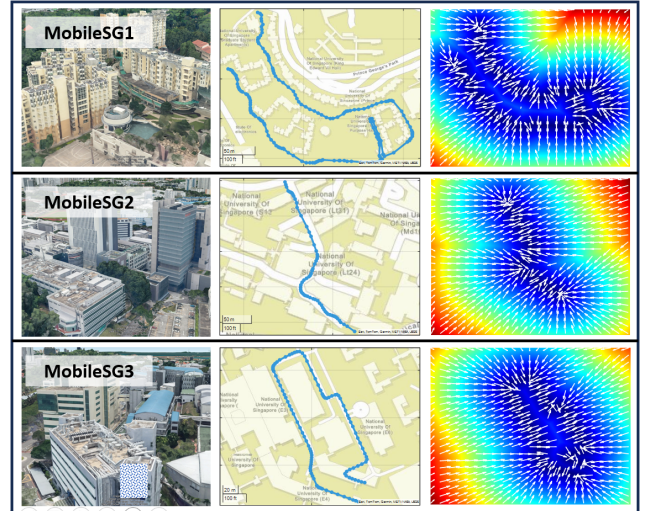


Figure 10: Three harsh urban scenes where we collected the MobileSG dataset to validate the EDF-based NeRC training.

Table 1: Dataset Description

Name	Urban Level	Train Num.	Test Num.	Length (km)	Phone Model	Label
GSDC21R	Light	200k	32k	120	Pixel4	3D
GSDC21U	Harsh	37k	15k	10	Pixel4	3D
GSDC22-1	Light	80k	41k	42	Pixel4	2D
GSDC22-2	Light	116k	14k	55	Pixel4	2D
GSDC23	Light	55k	9k	13	Pixel5	3D
MobileSG1	Harsh	43k	6k	0.9	K40	EDF
MobileSG2	Harsh	39k	2k	0.35	Mi9	EDF
MobileSG3	Harsh	41k	2k	0.5	X50	EDF

partition the dataset into two subsets: GSDC21R, containing data from rural areas, and GSDC21U, containing data from urban areas.

GSDC 2022: Google enhanced the quality of the datasets in the second year of the competition, particularly in terms of ground truth calibration [13]. However, the dataset only contains trajectories in open areas, where ranging measurement errors are trivial. Additionally, most traces in this dataset are annotated with only 2D location labels. We extract from it two subsets along two trajectories: GSDC22-1 and GSDC22-2.

GSDC 2023: The latest GSDC datasets offer similarly high-quality measurements as GSDC 2022, but with full 3D ground truth labels. From these, we extract a subset collected along a consistent route, referred to as GSDC23.

MobileSG: We collected a dataset in extremely challenging urban canyon areas using various Android devices, as illustrated in Figure 10. Ground truth locations were obtained only for the testing

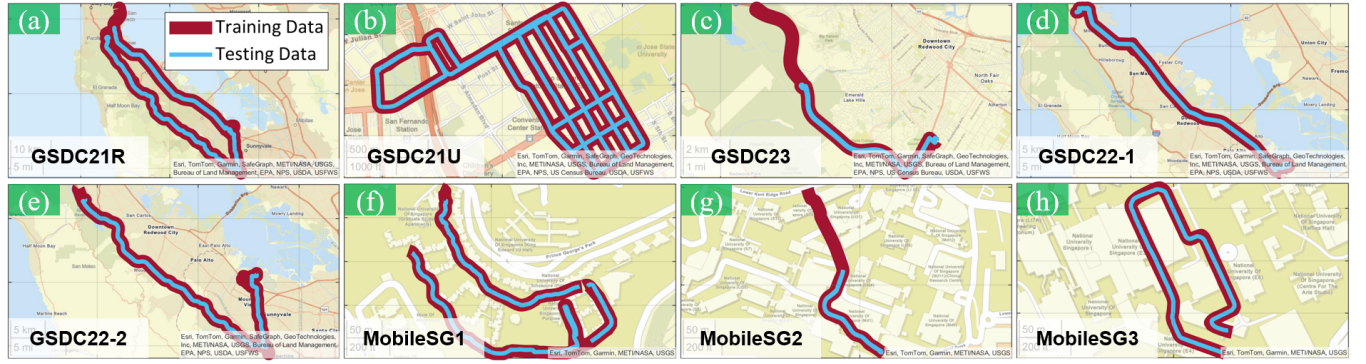


Figure 11: Visualization of datasets. (a) and (c)–(e) display open rural areas. (b) and (f)–(h) show densely urban canyons.

data, while the training data remained unlabeled. During testing data collection, the user’s movement was continuously recorded by a camera and later aligned with a 3D map in Google Earth Pro to determine the user’s locations [41]. This annotation method can achieve sub-meter accuracy [58], which is sufficient given that positioning errors in urban environments can reach up to several hundred meters [20]. As shown in Figure 10, the EDF cost map can be computed using publicly available street information corresponding to each training trajectory. The MobileSG dataset is used exclusively for evaluating the performance of EDF-based training.

Summary: The routes or scenes where all datasets were collected are visualized in Figure 11, spanning a diverse set of collection routes, ranging from rural to urban environments and covering both large-scale and small-scale scenarios.

6.2 Baseline Methods

We compare the proposed NeRC framework against both traditional model-based methods and state-of-the-art data-driven approaches.

Model-based methods: We choose the EKF, FGO (MHE-w/o-AC), and the full-information MHE (MHE-w/-AC) as baseline methods. To ensure a fair comparison, the covariance matrices and initial state are configured identically to those used in NeRC.

Learning-based methods using intermediate loss: FCNN-LSTM [93] and PrNet [81], two SOTA deep learning-based pseudorange correction methods, are selected as baseline models. As they only predict ranging corrections without providing localization results, we integrate them with an MHE-based positioning engine—identical to the downstream component used in NeRC. Notably, they require 3D location labels to retroactively compute the ranging errors. As a result, they are inapplicable to partially labeled or unlabeled datasets such as GSDC22 and MobileSG.

End-to-end learning: We also compared NeRC with SOTA end-to-end learning approaches, including the black-box GnssFormer and the structured learning paradigms E2E-PrNet [79] and pyrtklib [18, 22]. GnssFormer is our enhanced adaptation of the Set Transformer [28], incorporating the same input features used in NeRC and initialized with robust location estimates to guide its position corrections. Both E2E-PrNet and pyrtklib adopt the structure composed of an MLP followed by a differentiable WLS positioning engine. E2E-PrNet also leverages the Theseus library for differentiable optimization, while pyrtklib

integrates a differentiable Python binding of the popular `rtklib` library. We have enhanced these three baseline approaches with our proposed 2D and EDF-based training losses, enabling them to handle partially labeled or unlabeled data like NeRC. All the baseline methods we implemented or trained will be publicly available at: <https://github.com/AILocAR/NeRC>.

6.3 Results

Evaluation metrics: Most location-based mobile applications require only the device’s horizontal position. In the GSDC competitions, evaluation is conducted solely on the horizontal localization error, which is measured by the **horizontal distance** between the predicted and ground truth latitude/longitude coordinates. Accordingly, we evaluate only horizontal positioning performance in this work. The horizontal distance is calculated using Vincenty’s formulae [69], as implemented in the `pymap3d` library. Figure 12 illustrates the boxplots of horizontal errors of all the methods previously mentioned. Additionally, in accordance with the GSDC competition requirements, we report the **horizontal score** for each method, indicated by the red dot in Figure 12 and summarized in Table 2. The horizontal score is defined as the average of the 50th and 95th percentiles of the horizontal errors. A lower horizontal score indicates higher positioning accuracy.

Positioning performance: Figure 12 and Table 2 indicate that NeRC outperforms all baseline methods across all datasets.

(1) *Large-scale erroneous scenarios.* GSDC21R represents a large-scale erroneous scenario. As illustrated in Figure 11a, the data were collected along 120 km of open highways in the Bay Area, yet exhibit positioning errors of approximately 15 meters, as reflected in the model-based method results in Figure 12a. Despite the open-sky environment, such inaccuracies may stem from system-level issues, particularly ground truth calibration errors [13]. In this case, all data-driven methods perform well, with NeRC achieving horizontal accuracy comparable to FCNN-LSTM and PrNet.

(2) *Large-scale open scenarios.* GSDC22 and GSDC23 were collected in large-scale open-sky scenes where model-based baselines already achieve high localization accuracy (within 5 meters), owing to strong signal quality. In such environments, ranging errors are trivial and often comparable to the inherent measurement noise. As a result, methods like E2E-PrNet and pyrtklib tend to overfit the noise, leading to degraded performance. In contrast, NeRC,

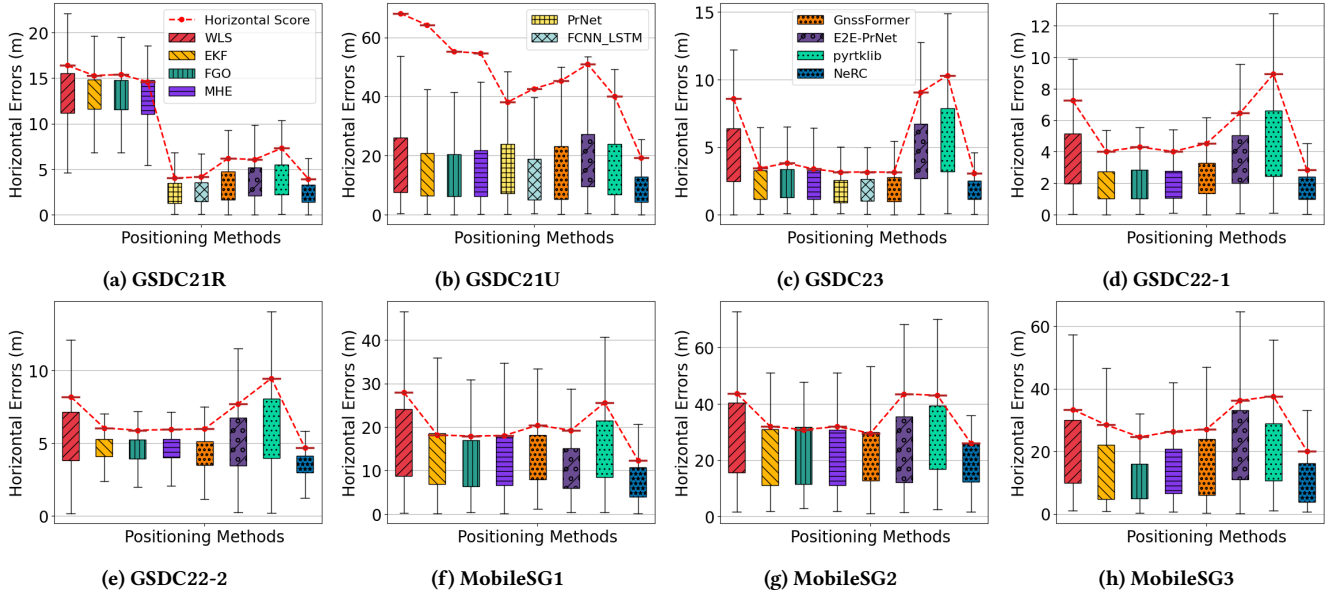


Figure 12: Horizontal positioning results.

supported by differentiable MHE, effectively suppresses noise and corrects residual ranging errors. GnssFormer, which directly regresses location corrections in a black-box fashion, is sensitive to its initialization quality—here, EKF estimates—around which its outputs fluctuate [46, 81]. With fully labeled data, PrNet and FCNN-LSTM can be trained on filtered ranging errors [81], which explains their performance approaching that of NeRC in Figure 12c. However, their reliance on complete 3D labeled data precludes their use on GSDC22, where only 2D location labels are available.

(3) *Small-scale urban canyons.* GSDC21U and MobileSG represent some of the most challenging small-scale urban localization scenarios. Despite severe multipath, NLOS effects, and high measurement noise, NeRC consistently outperforms all competing methods, achieving accuracy gains in both fully labeled and unlabeled settings. On the fully labeled GSDC21U dataset, NeRC surpasses the best model-based (MHE) and data-driven (PrNet) baselines by approximately 65% and 49%, respectively. On the unlabeled MobileSG dataset, NeRC improves over the leading model-based method (FGO) by 16–31% and outperforms data-driven approaches (E2E-PrNet and GnssFormer) by 12–36%. Therefore, NeRC reaches the SOTA level and maintains strong localization performance under these challenging conditions.

Impact of Training Methods: Figure 13a compares the effects of different training methods on the positioning errors of NeRC. The MHE algorithm is used as the baseline. The same MHE is also integrated into NeRC as the downstream localization engine to demonstrate NeRC’s improvement. The evaluation is conducted on GSDC21U. As shown Figure 13a, incorporating the EDF cost map can help reduce positioning errors without using ground-truth location data. Training with either 2D or 3D labels yields comparable performance, both contributing to further improvements in NeRC’s localization accuracy.

Overhead of Training and Inference: As illustrated in Figure 13b, we evaluate the computational time and GPU memory usage of end-to-end learning-based approaches during both training and inference. Compared to existing SOTA methods, our proposed NeRC generally introduces higher computational overhead, as it processes a horizon of measurements simultaneously. Among these methods, GnssFormer achieves the fastest training and inference speed, benefiting from PyTorch’s highly optimized Transformer implementation and its *precomputed* reference trajectories. In contrast, E2E-PrNet and NeRC exhibit longer running time due to repeatedly computing positions with a relatively less optimized nonlinear least squares solver [52]. Although pyrtklib leverages a standard MLP and a basic WLS algorithm, without involving any nonlinear solver, it incurs an even longer training time because it currently only supports sequential training [22]. About memory usage, although NeRC requires more resources during training, its memory consumption during inference is comparable to that of other methods. Its real-time performance will be further analyzed in section 7.

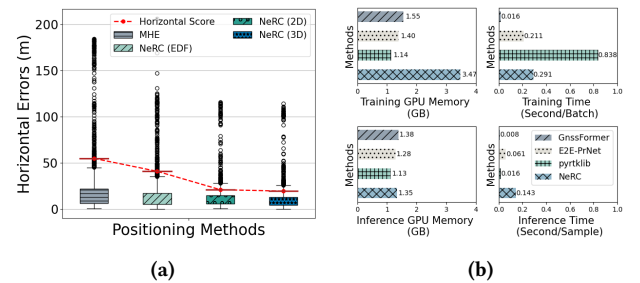


Figure 13: (a) Horizontal errors of NeRC trained using different losses. (b) Computational costs of end-to-end approaches

Table 2: Horizontal Scores (Meter \downarrow) in Different Datasets

Datasets			Model-based Methods				Intermediate Loss		End-to-end Learning			
			WLS	EKF	FGO	MHE	PrNet	FCNN-LSTM	GnssFormer	E2E-PrNet	pyrtklb	NeRC
3D	GSDC21	R	16.373	15.279	15.379	14.598	4.019	4.154	6.169	6.069	7.295	3.948
		U	68.136	64.201	55.190	54.705	38.071	42.714	45.314	50.959	40.180	19.301
	GSDC23	-	8.605	3.460	3.821	3.391	3.150	3.169	3.149	9.065	10.305	3.078
2D	GSDC22	1	7.248	4.025	4.299	4.010	\times	\times	4.522	6.448	8.934	2.837
		2	8.204	6.047	5.896	5.940	\times	\times	5.983	7.707	9.477	4.673
EDF	MobileSG	1	27.957	18.148	17.909	18.024	\times	\times	20.387	19.238	25.572	12.350
		2	43.687	31.992	30.824	31.948	\times	\times	29.570	43.525	43.002	26.043
		3	33.332	28.429	24.568	26.371	\times	\times	27.050	36.222	37.602	20.109

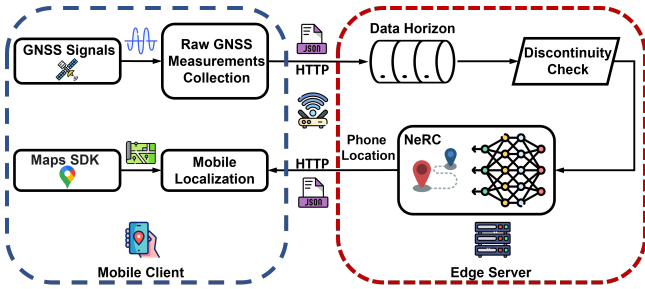


Figure 14: Edge-based mobile localization powered by NeRC

7 Real-Time Field Test

One potential real-world application of NeRC is to provide ranging correction services over a network when users enter GNSS-challenged environments [19, 41]. To this end, we design an edge-based mobile localization system powered by NeRC and evaluate its real-time performance in urban canyon areas characterized by dense high-rise buildings.

System Design: Figure 14 illustrates the diagram of the edge-based NeRC system for mobile positioning, which is a basic example of the client-server architecture. On the mobile client side, we developed an Android app to collect raw GNSS measurements and send them to the edge server via WLAN. Upon receiving data from smartphones, the edge server will cache it in a moving horizon, check for data discontinuities, and preprocess it for the subsequent neural ranging correction. Then, the server runs NeRC to compute user locations and send the results back to users via WLAN. By combining the map information accessed via the Google Maps API, we register user locations on 2D maps.

System Implementation: On the client side, we built the Android app in Java using Android Studio based on Google’s open-source software GnssLogger [12]. Raw GNSS measurements are collected with a frequency of 1 Hz via the Android Location API. Then, the collected data are packaged into JSON files for communicating with the edge server through the HTTP protocol [59]. The

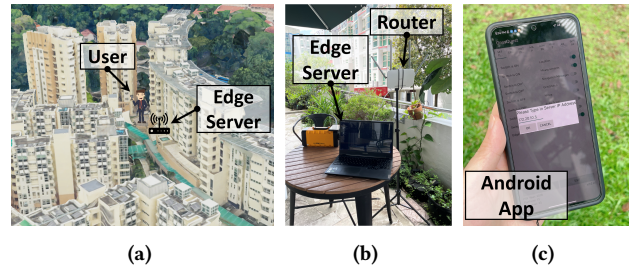


Figure 15: (a) The experiment scene. (b) The edge server and its wireless access point. (c) Client Android application.

app runs on an Android 13 phone powered by the Snapdragon 8+ Gen 1 processor with 12 GB RAM. Only the GPS L1 signals are utilized in our experiment.

The edge server is implemented using Uvicorn, an asynchronous web framework in Python, to listen and respond to requests from the Android client [9]. The received data are cached in a moving horizon, the size of which is tuned to 5. If the interval between the timestamps of the latest two messages is greater than 10 seconds, the data horizon will be considered discontinuous and reset to only hold the current message. The NeRC framework is implemented and trained in the same way as in the previous section, but is just running in inference mode [23]. The server runs Ubuntu 18.04.6 LTS, powered by an Intel Core i7-10750H 2.6 GHz CPU with 16 GB RAM and an NVIDIA GeForce RTX 2060 GPU.

Figure 15 illustrates the physical setup of the real-time test. The experiment was conducted in a densely built urban area, where a road was surrounded by high-rise buildings, as shown in Figure 15a. A user holding an Android phone walked along the road and localized himself using the NeRC system. As shown in Figure 15b, a 2.4 GHz wireless access point was installed on a second-floor balcony to provide the widest possible coverage and to connect the server and the user within the same WLAN. Our Android app, displayed in Figure 15c, enables communication with the server once the user inputs the server’s IP address.

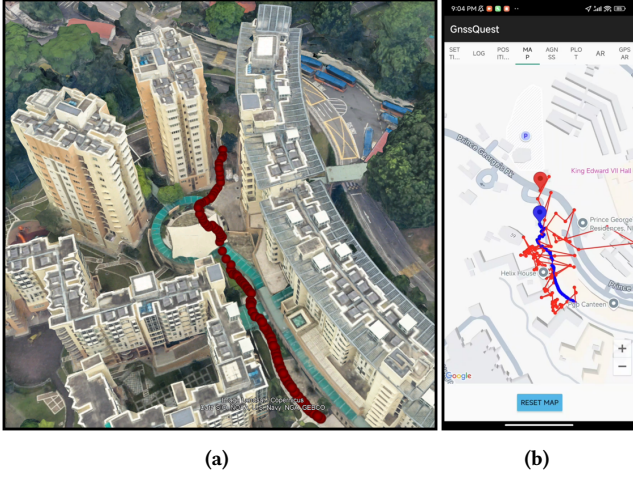


Figure 16: Real-time test. (a) The reference trajectory. (b) The real-time localization trajectories: the red trajectory is Google’s baseline solution, while the blue one is from NeRC. A complete screen record is available at: <https://www.bilibili.com/video/BV1CjgQzfEx8/>

System Profiling: This section focuses on quantitatively profiling the real-time performance of NeRC. Only a qualitative assessment of localization accuracy is provided here, as comprehensive evaluations on public and private benchmarks have already been presented in previous sections.

(1) *Localization accuracy.* The reference trajectory is scheduled ahead of time, as shown in Figure 16a. The user walked along the reference route, and the corresponding positioning result is presented in Figure 16b. The red trajectory in Figure 16b represents Google’s baseline solution provided by the open-source GnssLogger software [12]. Note that this is not the positioning result from the official Google Maps app, which utilizes in-phone GNSS chipset locations computed via the manufacturer’s proprietary algorithms. The baseline trajectory is visibly noisy and biased due to the severe multipath/NLOS propagation effects caused by the surrounding high-rise buildings. In contrast, NeRC’s solution, depicted in blue, closely follows the reference trajectory, demonstrating higher robustness and accuracy.

(2) *CPU overhead on mobile phones.* CPU and memory usage on the mobile device (Snapdragon 8+ Gen 1, 12 GB RAM) were measured using Android Studio’s live profiler [6, 85] under two conditions: with and without server connection. Figure 17 shows snapshots of the live profiling results. Our app, GnssQuest, demonstrates efficient performance in both cases. When the server is disconnected, average CPU usage is around 2%, peaking at 13%. The peak CPU usage is caused by map retrieval. Enabling the server connection adds only about 1% additional CPU load. Mean memory usage is approximately 280 MB without the server, increasing by just around 10 MB when the connection is active.

(3) *GPU overhead on the edge server.* The edge server running NeRC only performs in the inference mode, and the deployed neural model is trained offline in advance. We trigger “nvidia-smi” programmatically to log the usage of the server’s GPU and its memory

per second. The average usage of GPU memory across 123 samples is 1.4 GB, while the free GPU memory is up to 4.5 GB. Moreover, the average utilization of the GPU is just 4.8%. Thus, our NeRC model is lightweight enough to run on common consumer-level GPUs, such as the NVIDIA RTX 2060 we used.

(4) *Computational latency on the edge server.* We logged the inference time of NeRC on the edge server to evaluate its computational efficiency. On average, computing a location from a single epoch of measurements takes 100 ms, with a median latency of 98 ms. The inference time is closely influenced by the size of the neural network, the horizon length used in the MHE, and the performance of the GPU. Using a smaller neural network or horizon size on a more powerful GPU can reduce the latency.

(5) *End-to-end latency.* We define the end-to-end latency as the time interval required for the app to send raw measurements to the edge server and receive the localization results in return [7, 9]. Accordingly, we measured this latency on the client side. The end-to-end latency includes both the server-side computation time and the communication delay over the WLAN. In our experiment, the mean end-to-end latency was 246 ms, and the median was 225 ms. Given that our system operates at 1 Hz (i.e., Android collects raw GNSS measurements once per second), this level of latency has a negligible impact on the system’s real-time performance.

8 Related Work

We review related work about ranging error correction for GNSS, moving horizon estimation, and end-to-end structured learning.

Correcting Ranging Errors for GNSS: Correcting multipath and NLOS-induced pseudorange errors can significantly enhance GNSS positioning, but existing solutions often require 3D city models [41, 45] or additional sensors such as fisheye cameras or LiDAR [2, 76], limiting widespread deployment. An alternative line of research uses deep learning to regress ranging errors directly from **only** raw GNSS measurements. While promising, state-of-the-art methods either depend on complex intermediate-loss **estimation** from fully labeled data [62, 65, 81, 93] or learn via a basic WLS engine [22, 79], making them label-intensive or noise-sensitive. We address these limitations with a neural ranging correction framework that learns from widely available raw GNSS measurements through a differentiable, noise-resilient location estimator. Moreover, by incorporating basic 2D public maps, our method opens opportunities for leveraging ubiquitous unlabeled GNSS data.

Moving Horizon Estimation: MHE is a well-established state estimation method effective for both linear [34, 48] or nonlinear

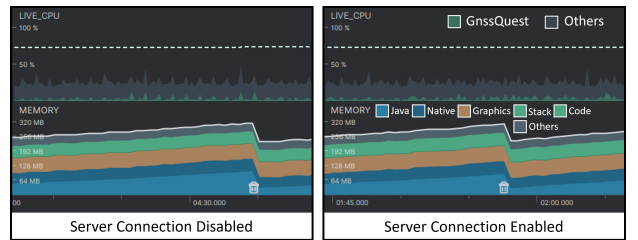


Figure 17: CPU and memory usage (an Android 13 phone with Snapdragon 8+ Gen 1, 12GB RAM)

[53, 55, 56, 82] systems under the least-squares framework. It has been successfully applied in diverse domains, including chemical process control [54, 88], agriculture [32], satellite control [96], and robotics [11, 27, 70, 71]. More recently, its use in satellite navigation has also been explored [36, 37, 74, 80, 82]. Meanwhile, as an equivalent version of MHE under the assumption of Gaussian system statistics [82], FGO has also demonstrated outstanding performance in positioning using raw GNSS measurements [38, 66, 75, 86, 87]. However, prior studies have not examined the performance of MHE when integrated into a learning pipeline, particularly regarding its forward and backward performance. Our work addresses this gap.

End-to-end Structured Learning: The learning paradigm that integrates data-driven neural modules and differentiable physical reasoning has been widely adopted in robotics [4, 30, 70, 71], autonomous driving [24, 35], 3D vision [5, 68], optical [44] and radio frequency reconstruction [97, 98], as well as other domains requiring physical or logical priors [52]. This paradigm has also been formalized under the high-level concept of **Imperative Learning** [72], with applications in path planning [89], feature matching [91], and simultaneous localization and mapping (SLAM) [14]. Recent studies have brought this idea to GNSS localization, including end-to-end learning-based LOS/NLOS signal weighting [86, 87] and ranging error correction [22, 79]. In the context of ranging error regression, existing methods have so far relied solely on a baseline WLS localization engine and have been trained using fully labeled data with 3D ground truth [22, 79]. In this paper, we address both limitations by introducing a differentiable, noise-resilient location estimator and enabling training with unlabeled data.

9 Conclusion, Limitations, and Future Work

This paper presents NeRC, a novel neural ranging correction framework designed to enhance GNSS localization for mobile devices. NeRC is trained through differentiable moving horizon location estimation, guided by a final location-based loss to ensure end-to-end optimization. Based on this learning pipeline, we propose a new paradigm that leverages unlabeled GNSS data by incorporating Euclidean distance supervision derived from publicly available maps. Extensive evaluations on both public and private benchmarks demonstrate the robustness and superiority of NeRC across rural and urban environments under both labeled and unlabeled settings. NeRC has reached the SOTA level. Furthermore, an edge-based field test reveals its promising potential for practical deployment.

The following limitations of NeRC merit further investigation:

(1) From centralized to distributed: NeRC is currently trained offline using pre-collected datasets on a high-performance workstation. To harness ubiquitous data and computational resources, training NeRC in a distributed way is a worthwhile direction [8].

(2) From deep learning to pretraining: NeRC learns from unlabeled data under the assumption that we know the reference routes along which the data were collected. Exploiting more general crowdsourced unlabeled GNSS data with minimal prior knowledge could pave the way for pretraining GNSS foundation models [60].

(3) From fingerprinting to generalization: NeRC is currently designed to regress ranging errors of satellites observed in the same location during similar periods of days. Incorporating other sensing modalities shows potentials for generalizable error modeling [78].

Acknowledgments

This paper was supported by Nanyang Technological University under the NTU Research Scholarship:~R2015378 (<https://www.ntu.edu.sg/admissions/graduate/financialmatters/scholarships/rss>).

References

- [1] Penina Axelrad, Kristine Larson, and Brandon Jones. 2005. Use of the correct satellite repeat period to characterize and reduce site-specific multipath errors. In *Proceedings of the 18th International Technical Meeting of the Satellite Division of the Institute of Navigation (ION GNSS 2005)*. Institute of Navigation, 2638–2648.
- [2] Xiwei Bai, Weisong Wen, and Li-ta Hsu. 2020. Using Sky-pointing fish-eye camera and LiDAR to aid GNSS single-point positioning in urban canyons. *IET Intelligent Transport Systems* 14, 8 (2020), 908–914.
- [3] Heinz Breu, Joseph Gil, David Kirkpatrick, and Michael Werman. 1995. Linear time Euclidean distance transform algorithms. *IEEE Transactions on Pattern Analysis and Machine Intelligence* 17, 5 (1995), 529–533.
- [4] Kun Cao, Xinhang Xu, Wanxin Jin, Karl H Johansson, and Lihua Xie. 2024. A differential dynamic programming framework for inverse reinforcement learning. *arXiv preprint arXiv:2407.19902* (2024).
- [5] Hansheng Chen, Pichai Wang, Fan Wang, Wei Tian, Lu Xiong, and Hao Li. 2022. Epro-pnp: Generalized end-to-end probabilistic perspective-n-points for monocular object pose estimation. In *Proceedings of the IEEE/CVF Conference on Computer Vision and Pattern Recognition*. 2781–2790.
- [6] Ying Chen, Sasamon Omoma, Hojung Kwon, Hazer Inaltekin, and Maria Gorlatova. 2024. Quantifying and Exploiting VR Frame Correlations: An Application of a Statistical Model for Viewport Pose. *IEEE Transactions on Mobile Computing* 23, 12 (2024), 11466–11482.
- [7] Shiyi Ding and Ying Chen. 2025. RAG-VR: Leveraging Retrieval-Augmented Generation for 3D Question Answering in VR Environments. In *2025 IEEE Conference on Virtual Reality and 3D User Interfaces Abstracts and Workshops (VRW)*. IEEE, 131–136.
- [8] Yao Du, Zehua Wang, Cyril Leung, and Victor CM Leung. 2023. Accelerating and securing blockchain-enabled distributed machine learning. *IEEE Transactions on Mobile Computing* 23, 6 (2023), 6712–6730.
- [9] Lin Duan, Ying Chen, Zhehan Qu, Megan McGrath, Erin Ehmke, and Maria Gorlatova. 2024. BiGuide: A bi-level data acquisition guidance for object detection on mobile devices. In *2024 23rd ACM/IEEE International Conference on Information Processing in Sensor Networks (IPSN)*. IEEE, 88–100.
- [10] Pedro F Felzenszwalb and Daniel P Huttenlocher. 2012. Distance transforms of sampled functions. *Theory of computing* 8, 1 (2012), 415–428.
- [11] Felix Fiedler, Dirk Baumbach, Anko Börner, and Sergio Lucia. 2020. A probabilistic moving horizon estimation framework applied to the visual-inertial sensor fusion problem. In *2020 European Control Conference (ECC)*. IEEE, 1009–1016.
- [12] Guoyu Michael Fu, Mohammed Khider, and Frank Van Diggelen. 2020. Android raw GNSS measurement datasets for precise positioning. In *Proceedings of the 33rd international technical meeting of the satellite division of the Institute of Navigation (ION GNSS+ 2020)*. 1925–1937.
- [13] Michael Fu, Mohammed Khider, and Frank Van Diggelen. 2022. Summary and legacy of the smartphone decimeter challenge (sdc) 2022. In *Proceedings of the 35th International Technical Meeting of the Satellite Division of The Institute of Navigation (ION GNSS+ 2022)*. 2301–2320.
- [14] Taimeng Fu, Shaoshu Su, Yiren Lu, and Chen Wang. 2024. islam: Imperative slam. *IEEE Robotics and Automation Letters* 9, 5 (2024), 4607–4614.
- [15] Luxin Han, Fei Gao, Boyu Zhou, and Shaojie Shen. 2019. Fiesta: Fast incremental euclidean distance fields for online motion planning of aerial robots. In *2019 IEEE/RSJ International Conference on Intelligent Robots and Systems (IROS)*. IEEE, 4423–4430.
- [16] Eric L Haseltine and James B Rawlings. 2005. Critical evaluation of extended Kalman filtering and moving-horizon estimation. *Industrial & engineering chemistry research* 44, 8 (2005), 2451–2460.
- [17] Kaiming He, Xiangyu Zhang, Shaoqing Ren, and Jian Sun. 2015. Delving deep into rectifiers: Surpassing human-level performance on imagenet classification. In *Proceedings of the IEEE international conference on computer vision*. 1026–1034.
- [18] Jorge Hernández Olcina, Ana B Anquela Julián, and Ángel E Martín Furones. 2024. Python toolbox for Android GNSS raw data to RINEX conversion. *GPS Solutions* 28, 2 (2024), 95.
- [19] Jorge Hernández Olcina, Ana B Anquela Julián, and Ángel E Martín Furones. 2024. Real-time cloud computing of GNSS measurements from smartphones and mobile devices for enhanced positioning and navigation. *GPS Solutions* 28, 4 (2024), 167.
- [20] Li-Ta Hsu. 2018. Analysis and modeling GPS NLOS effect in highly urbanized area. *GPS Solutions* 22, 1 (2018), 7. doi:10.1007/s10291-017-0667-9
- [21] Li-Ta Hsu, Feng Huang, Hoi-Fung Ng, Guohao Zhang, Yihan Zhong, Xiwei Bai, and Weisong Wen. 2023. Hong Kong UrbanNav: An open-source multisensory dataset for benchmarking urban navigation algorithms. *NAVIGATION: Journal of*

the Institute of Navigation 70, 4 (2023).

[22] Runzhi Hu, Penghui Xu, Yihan Zhong, and Weisong Wen. 2025. pyrtklib: An open-source package for tightly coupled deep learning and GNSS integration for positioning in urban canyons. *IEEE Transactions on Intelligent Transportation Systems* (2025).

[23] Tianyi Hu, Tim Scargill, Fan Yang, Ying Chen, Guohao Lan, and Maria Gorlatova. 2024. SEESys: Online pose error estimation system for visual SLAM. In *Proceedings of the 22nd ACM Conference on Embedded Networked Sensor Systems*. 322–335.

[24] Zhiyu Huang, Haochen Liu, Jingda Wu, and Chen Lv. 2023. Differentiable integrated motion prediction and planning with learnable cost function for autonomous driving. *IEEE transactions on neural networks and learning systems* 35, 11 (2023), 15222–15236.

[25] Zhiyu Huang, Haochen Liu, Jingda Wu, and Chen Lv. 2024. Differentiable Integrated Motion Prediction and Planning With Learnable Cost Function for Autonomous Driving. *IEEE Transactions on Neural Networks and Learning Systems* 35, 11 (2024), 15222–15236. doi:10.1109/TNNLS.2023.3283542

[26] AH Jazwinski. 1970. *Stochastic processes and filtering theory*. ACADEMIC PRESS, INC.,.

[27] Jiarong Kang, Yi Wang, and Xiaobin Xiong. 2024. Fast decentralized state estimation for legged robot locomotion via EKF and MHE. *IEEE Robotics and Automation Letters* (2024).

[28] Ashwin V Kanhere, Shubh Gupta, Akshay Shetty, and Grace Gao. 2022. Improving gnss positioning using neural-network-based corrections. *NAVIGATION: Journal of the Institute of Navigation* 69, 4 (2022).

[29] Elliott D Kaplan and Christopher Hegarty. 2017. *Understanding GPS/GNSS: Principles and Applications*. Artech house.

[30] Chunshang Li and Steven L Waslander. 2020. Towards end-to-end learning of visual inertial odometry with an EKF. In *2020 17th Conference on Computer and Robot Vision (CRV)*. IEEE Computer Society, 190–197.

[31] Guangcai Li and Jianghui Geng. 2019. Characteristics of raw multi-GNSS measurement error from Google Android smart devices. *GPS Solutions* 23, 3 (2019), 90.

[32] Xiaojie Li, Song Bo, Xuewen Zhang, Yan Qin, and Xunyuan Yin. 2024. Data-driven parallel Koopman subsystem modeling and distributed moving horizon state estimation for large-scale nonlinear processes. *AICHE Journal* 70, 3 (2024), e18326.

[33] Keck Voon Ling and Khiang Wee Lim. 1996. A state space GPC with extensions to multirate control. *Automatica* 32, 7 (1996), 1067–1071.

[34] Keck Voon Ling and Khiang Wee Lim. 1999. Receding horizon recursive state estimation. *IEEE Trans. Automat. Control* 44, 9 (1999), 1750–1753. doi:10.1109/9.788546

[35] Haochen Liu, Zhiyu Huang, Wenhui Huang, Haohan Yang, Xiaoyu Mo, and Chen Lv. 2025. Hybrid-prediction integrated planning for autonomous driving. *IEEE Transactions on Pattern Analysis and Machine Intelligence* (2025).

[36] Peng Liu, Keck Voon Ling, Honglei Qin, Muyuan Jiang, and Jun Lu. 2024. Actualization analysis of LEO opportunistic doppler aided GNSS precise point positioning using moving horizon estimation. *IEEE Transactions on Vehicular Technology* 73, 7 (2024), 9453–9464.

[37] Peng Liu, Keck Voon Ling, Honglei Qin, and Jun Lu. 2023. State-space-varied moving horizon estimation for real-time PPP in the challenging low-cost antenna and chipset. *GPS Solutions* 27, 4 (2023), 161.

[38] Peng Liu, Honglei Qin, Jun Lu, Muyuan Jiang, Yong Liang Guan, and Chau Yuen. 2025. Attitude Bound-Constrained Factor Graph Optimization for GNSS and IMU Fusion Positioning in Bumpy Scenarios. *IEEE Transactions on Instrumentation and Measurement* (2025).

[39] Wanke Liu, Xiang Shi, Feng Zhu, Xianlu Tao, and Fuhong Wang. 2019. Quality analysis of multi-GNSS raw observations and a velocity-aided positioning approach based on smartphones. *Advances in Space Research* 63, 8 (2019), 2358–2377.

[40] Xiaochen Liu, Suman Nath, and Ramesh Govindan. 2018. Gnome: A Practical Approach to NLOS Mitigation for GPS Positioning in Smartphones. In *Proceedings of the 16th Annual International Conference on Mobile Systems, Applications, and Services* (Munich, Germany) (*MobiSys '18*). Association for Computing Machinery, New York, NY, USA, 163–177. doi:10.1145/3210240.3210343

[41] Xiaochen Liu, Suman Nath, and Ramesh Govindan. 2018. Gnome: A practical approach to NLOS mitigation for GPS positioning in smartphones. In *Proceedings of the 16th Annual International Conference on Mobile Systems, Applications, and Services*. Association for Computing Machinery, New York, NY, USA, 163–177. doi:10.1145/3210240.3210343

[42] Zhidan Liu, Jiancong Liu, Xiaowen Xu, and Kaishun Wu. 2022. DeepGPS: Deep learning enhanced GPS positioning in urban canyons. *IEEE Transactions on Mobile Computing* 23, 1 (2022), 376–392.

[43] Calvin R Maurer, Rensheng Qi, and Vijay Raghavan. 2003. A linear time algorithm for computing exact Euclidean distance transforms of binary images in arbitrary dimensions. *IEEE Transactions on Pattern Analysis and Machine Intelligence* 25, 2 (2003), 265–270.

[44] Ben Mildenhall, Pratul P. Srinivasan, Matthew Tancik, Jonathan T. Barron, Ravi Ramamoorthi, and Ren Ng. 2020. NeRF: Representing Scenes as Neural Radiance Fields for View Synthesis. In *Computer Vision – ECCV 2020*, Andrea Vedaldi, Horst Bischof, Thomas Brox, and Jan-Michael Frahm (Eds.). Springer International Publishing, Cham, 405–421.

[45] Shunsuke Miura, Li-Ta Hsu, Feiyu Chen, and Shunsuke Kamijo. 2015. GPS error correction with pseudorange evaluation using three-dimensional maps. *IEEE Transactions on Intelligent Transportation Systems* 16, 6 (2015), 3104–3115.

[46] Adyasha Mohanty and Grace Gao. 2023. Learning GNSS positioning corrections for smartphones using graph convolution neural networks. *NAVIGATION: Journal of the Institute of Navigation* 70, 4 (2023).

[47] Y Jade Morton, Frank van Diggelen, James J Spilker Jr, Bradford W Parkinson, Sherman Lo, and Grace Gao. 2021. *Position, navigation, and timing technologies in the 21st century: Integrated satellite navigation, sensor systems, and civil applications, volume 1*. John Wiley & Sons.

[48] Kenneth R Muske, James B Rawlings, and Jay H Lee. 1993. Receding horizon recursive state estimation. In *1993 American Control Conference*. IEEE, San Francisco, CA, USA, 900–904. doi:10.23919/ACC.1993.4792993

[49] Hoi-fung Ng, Guohai Zhang, Yiran Luo, and Li-ta Hsu. 2021. Urban positioning: 3D mapping-aided GNSS using dual-frequency pseudorange measurements from smartphones. *Navigation* 68, 4 (2021), 727–749.

[50] David W Paglieroni. 1992. Distance transforms: Properties and machine vision applications. *CVGIP: Graphical models and image processing* 54, 1 (1992), 56–74.

[51] Quoc-Huy Phan, Su-Lim Tan, and Ian McLoughlin. 2013. GPS multipath mitigation: a nonlinear regression approach. *GPS Solutions* 17, 3 (2013), 371–380.

[52] Luis Pineda, Taosha Fan, Maurizio Monge, Shobha Venkataraman, Paloma Sodhi, Ricky TQ Chen, Joseph Ortiz, Daniel DeTone, Austin Wang, Stuart Anderson, et al. 2022. Theseus: A library for differentiable nonlinear optimization. *Advances in Neural Information Processing Systems* 35 (2022), 3801–3818.

[53] Christopher V Rao and James B Rawlings. 2000. Nonlinear moving horizon state estimation. In *Nonlinear Model Predictive Control*. Springer, 45–69.

[54] Christopher V Rao and James B Rawlings. 2002. Constrained process monitoring: Moving-horizon approach. *AICHE Journal* 48, 1 (2002), 97–109.

[55] Christopher V Rao, James B Rawlings, and Jay H Lee. 2001. Constrained linear state estimation—a moving horizon approach. *Automatica* 37, 10 (2001), 1619–1628.

[56] Christopher V Rao, James B Rawlings, and David Q Mayne. 2003. Constrained state estimation for nonlinear discrete-time systems: Stability and moving horizon approximations. *IEEE Trans. Automat. Control* 48, 2 (2003), 246–258.

[57] Nathan Ratliff, Matt Zucker, J Andrew Bagnell, and Siddhartha Srinivasa. 2009. CHOMP: Gradient optimization techniques for efficient motion planning. In *2009 IEEE International Conference on Robotics and Automation*. IEEE, 489–494.

[58] Paul-Edouard Sarlin, Daniel DeTone, Tsun-Yi Yang, Armen Avetisyan, Julian Straub, Tomasz Malisiewicz, Samuel Rota Bulo, Richard Newcombe, Peter Kortschieder, and Vasileios Balntas. 2023. Orienternet: Visual localization in 2d public maps with neural matching. In *Proceedings of the IEEE/CVF Conference on Computer Vision and Pattern Recognition*. 21632–21642.

[59] Tim Scargill, Ying Chen, Tianyi Hu, and Maria Gorlatova. 2023. SiTAR: Situated trajectory analysis for in-the-wild pose error estimation. In *2023 IEEE International Symposium on Mixed and Augmented Reality (ISMAR)*. IEEE, 283–292.

[60] Jamie Smith, Anton Kast, Anton Geraschenko, Y Jade Morton, Michael P Brenner, Frank van Diggelen, and Brian P Williams. 2024. Mapping the ionosphere with millions of phones. *Nature* 635, 8038 (2024), 365–369.

[61] James J Spilker Jr, Penina Axelrad, Bradford W Parkinson, and Per Enge. 1996. *Global positioning system: theory and applications, volume I*. American Institute of Aeronautics and Astronautics.

[62] Rui Sun, Linxia Fu, Qi Cheng, Kai-Wei Chiang, and Wu Chen. 2023. Resilient pseudorange error prediction and correction for GNSS positioning in urban areas. *IEEE Internet of Things Journal* 10, 11 (2023), 9979–9988.

[63] Rui Sun, Linxia Fu, Guanyu Wang, Qi Cheng, Li-Ta Hsu, and Washington Yotto Ochieng. 2021. Using dual-polarization GPS antenna with optimized adaptive neuro-fuzzy inference system to improve single point positioning accuracy in urban canyons. *Navigation* 68, 1 (2021), 41–60.

[64] Rui Sun, Qi Cheng, Qi Cheng, Xiaotong Shang, and Washington Yotto Ochieng. 2025. 3D Grid-Based Resilient Pseudorange Error Prediction for Adaptive GNSS/IMU Integrated Navigation in Urban Areas. *IEEE Internet of Things Journal* (2025).

[65] Rui Sun, Guanyu Wang, Qi Cheng, Linxia Fu, Kai-Wei Chiang, Li-Ta Hsu, and Washington Yotto Ochieng. 2020. Improving GPS code phase positioning accuracy in urban environments using machine learning. *IEEE Internet of Things Journal* 8, 8 (2020), 7065–7078.

[66] Taro Suzuki. 2023. Precise position estimation using smartphone raw GNSS data based on two-step optimization. *Sensors* 23, 3 (2023), 1205.

[67] Matthew J Tenny and James B Rawlings. 2002. Efficient moving horizon estimation and nonlinear model predictive control. In *Proceedings of the 2002 American Control Conference (IEEE Cat. No. CH37301)*, Vol. 6. IEEE, 4475–4480.

[68] Eugene Valassakis and Guillermo Garcia-Hernando. 2024. Handdgp: Camera-space hand mesh prediction with differentiable global positioning. In *European Conference on Computer Vision*. Springer, 479–496.

[69] Thaddeus Vincenty. 1975. Direct and inverse solutions of geodesics on the ellipsoid with application of nested equations. *Survey review* 23, 176 (1975), 88–93.

[70] Bingheng Wang, Zhengtian Ma, Shupeng Lai, and Lin Zhao. 2024. Neural Moving Horizon Estimation for Robust Flight Control. *IEEE Transactions on Robotics* 40 (2024), 639–659. doi:10.1109/TRO.2023.3331064

[71] Bingheng Wang, Zhengtian Ma, Shupeng Lai, Lin Zhao, and Tong Heng Lee. 2021. Differentiable moving horizon estimation for robust flight control. In *2021 60th IEEE Conference on Decision and Control (CDC)*. IEEE, 3563–3568.

[72] Chen Wang, Kaiyi Ji, Junyi Geng, Zhongqiang Ren, Taimeng Fu, Fan Yang, Yifan Guo, Haonan He, Xiangyu Chen, Zitong Zhan, Qiwei Du, Shaoshu Su, Bowen Li, Yuheng Qiu, Yi Du, Qihang Li, Yifan Yang, Xiao Lin, and Zhipeng Zhao. 2025. Imperative learning: A self-supervised neuro-symbolic learning framework for robot autonomy. *The International Journal of Robotics Research* 0, 0 (2025), 1–40. doi:10.1177/02783649251353181

[73] Lei Wang, Paul D Groves, and Marek K Ziebart. 2015. Smartphone shadow matching for better cross-street GNSS positioning in urban environments. *The Journal of Navigation* 68, 3 (2015), 411–433.

[74] Yang Wang, Rong Yang, Keck Voon Ling, and Eng Kee Poh. 2015. Robust vector tracking loop using moving horizon estimation. In *Proceedings of the ION 2015 Pacific PNT Meeting*. 640–648.

[75] Weisong Wen, Tim Pfeifer, Xiwei Bai, and Li-Ta Hsu. 2021. Factor graph optimization for GNSS/INS integration: A comparison with the extended Kalman filter. *NAVIGATION: Journal of the Institute of Navigation* 68, 2 (2021), 315–331.

[76] Weisong Wen, Guohao Zhang, and Li-Ta Hsu. 2019. Correcting NLOS by 3D LiDAR and building height to improve GNSS single point positioning. *Navigation* 66, 4 (2019), 705–718.

[77] Duojie Weng, Zhiyu Hou, Yang Meng, Miaomiao Cai, and Yanyiu Chan. 2023. Characterization and mitigation of urban GNSS multipath effects on smartphones. *Measurement* 223 (2023), 113766.

[78] Xu Weng, Yuhui Jin, and KV Ling. 2024. GnssQuest: Questing for Suitable GNSS Satellites through Augmented Reality. In *Proceedings of the 22nd ACM Conference on Embedded Networked Sensor Systems*. 867–868.

[79] Xu Weng, K.V. Ling, Haochen Liu, and Kun Cao. 2024. Towards End-to-End GPS Localization with Neural Pseudorange Correction. In *2024 27th International Conference on Information Fusion (FUSION)*. 1–7. doi:10.23919/FUSION59988.2024.10706359

[80] Xu Weng and Keck Voon Ling. 2023. Localization with noisy Android raw GNSS measurements. In *2023 IEEE Asia Pacific Conference on Wireless and Mobile (APWiMob)*. IEEE, 95–101.

[81] Xu Weng, K. V. Ling, and Haochen Liu. 2024. PrNet: A Neural Network for Correcting Pseudoranges to Improve Positioning With Android Raw GNSS Measurements. *IEEE Internet of Things Journal* 11, 14 (2024), 24973–24983. doi:10.1109/JIOT.2024.3392302

[82] Xu Weng, K. V. Ling, and Ling Zhao. 2025. Receding Horizon Recursive Location Estimation. arXiv:2506.18430 [eess.SY] <https://arxiv.org/abs/2506.18430>

[83] Xiao Xia, Weisong Wen, and Li-Ta Hsu. 2024. Integrity-Constrained Factor Graph Optimization for GNSS Positioning in Urban Canyons. *NAVIGATION: Journal of the Institute of Navigation* 71, 3 (2024).

[84] Bing Xu, Qiongqiong Jia, Yiran Luo, and Li-Ta Hsu. 2019. Intelligent GPS L1 LOS/multipath/NLOS classifiers based on correlator-, RINEX-and NMEA-level measurements. *Remote Sensing* 11, 16 (2019), 1851.

[85] Huatao Xu, Pengfei Zhou, Rui Tan, and Mo Li. 2023. Practically adopting human activity recognition. In *Proceedings of the 29th Annual International Conference on Mobile Computing and Networking*. 1–15.

[86] Penghui Xu and Li-Ta Hsu. 2024. AutoW: Self-Supervision Learning for Weighting Estimation in GNSS Positioning. In *Proceedings of the 37th International Technical Meeting of the Satellite Division of The Institute of Navigation (ION GNSS+ 2024)*. 2630–2644.

[87] Penghui Xu, Hoi-Fung Ng, Yihan Zhong, Guohao Zhang, Weisong Wen, Bo Yang, and Li-Ta Hsu. 2023. Differentiable factor graph optimization with intelligent covariance adaptation for accurate smartphone positioning. In *Proceedings of the 36th International Technical Meeting of the Satellite Division of The Institute of Navigation (ION GNSS+ 2023)*. 2765–2773.

[88] Mingxue Yan, Minghao Han, Adrian Wing-Keung Law, and Xunyuan Yin. 2025. Self-tuning moving horizon estimation of nonlinear systems via physics-informed machine learning Koopman modeling. *AIChE Journal* 71, 2 (2025), e18649.

[89] Fan Yang, Chen Wang, Cesar Cadena, and Marco Hutter. 2023. iPlanner: Imperative Path Planning. In *Robotics: Science and Systems (RSS)*. <https://arxiv.org/abs/2302.11434>

[90] Fan Yang, Chen Wang, Cesar Cadena, and Marco Hutter. 2023. iPlanner: Imperative Path Planning. In *Proceedings of Robotics: Science and Systems*. Daegu, Republic of Korea. doi:10.15607/RSS.2023.XIX.064

[91] Zitong Zhan, Dasong Gao, Yun-Jou Lin, Youjie Xia, and Chen Wang. 2024. iMatching: Imperative correspondence learning. In *European Conference on Computer Vision*. Springer, 183–200.

[92] Aston Zhang, Zachary C Lipton, Mu Li, and Alexander J Smola. 2023. *Dive into deep learning*. Cambridge University Press.

[93] Guohao Zhang, Penghui Xu, Haosheng Xu, and Li-Ta Hsu. 2021. Prediction on the Urban GNSS Measurement Uncertainty Based on Deep Learning Networks With Long Short-Term Memory. *IEEE Sensors Journal* 21, 18 (2021), 20563–20577. doi:10.1109/JSEN.2021.3098006

[94] Xiaohong Zhang, Xianlu Tao, Feng Zhu, Xiang Shi, and Fuhong Wang. 2018. Quality assessment of GNSS observations from an Android N smartphone and positioning performance analysis using time-differenced filtering approach. *Gps Solutions* 22 (2018), 1–11.

[95] Haoli Zhao, Zhenhui Li, Qianming Wang, Kan Xie, Shengli Xie, Ming Liu, and Ci Chen. 2024. Improving performances of GNSS positioning correction using multiview deep reinforcement learning with sparse representation. *GPS Solutions* 28, 3 (2024), 98.

[96] Ling Zhao, Zhengliang Lu, Keck Voon Ling, Yuandong Hu, Kan Zheng, and Wenhe Liao. 2025. Multi-rate Cascade Spacecraft Attitude-Orbit Integrated State Estimation and Control Framework based on MHE and PWA-MPC. *IEEE Trans. Aerospace Electron. Systems* (2025).

[97] Xiaopeng Zhao, Zhenlin An, Qingrui Pan, and Lei Yang. 2023. Nerf2: Neural radio-frequency radiance fields. In *Proceedings of the 29th Annual International Conference on Mobile Computing and Networking*. 1–15.

[98] Xiaopeng Zhao, Shen Wang, Zhenlin An, and Lei Yang. 2024. Crowdsourced Geospatial Intelligence: Constructing 3D Urban Maps with Satellitic Radiance Fields. *Proceedings of the ACM on Interactive, Mobile, Wearable and Ubiquitous Technologies* 8, 3 (2024), 1–24.

[99] Yihan Zhong, Weisong Wen, Hoi-Fung Ng, Xiwei Bai, and Li-Ta Hsu. 2022. Real-time factor graph optimization aided by graduated non-convexity based outlier mitigation for smartphone decimeter challenge. In *Proceedings of the 35th International Technical Meeting of the Satellite Division of The Institute of Navigation (ION GNSS+ 2022)*. 2339–2348.

Received 20 February 2007; revised 12 March 2009; accepted 5 June 2009